Modelling of sawtooth-induced fast ion transport in positive and negative triangularity in TCV

Matteo Vallar[1], Mario Podestà[2], Marcelo Baquero-Ruiz[1], Philip Bonofiglio[2], Basil Duval[1], Alexander N. Karpushov[1], Antoine Merle[1], Dmytry Mikitchuk[1], Olivier Sauter[1], Lorenzo Stipani[1], Duccio Testa[1], and the TCV team[3]

[1]Ecole Polytechnique Fédérale de Lausanne (EPFL), Swiss Plasma Center (SPC), CH-1015 Lausanne, Switzerland
[2]Princeton Plasma Physics Laboratory, Princeton, New Jersey 08543, USA
[3]See Coda et al 2019 (https://doi.org/10.1088/1741-4326/ab25cb) for the TCV team.

November 10, 2021

Abstract

Internal kinks are a common magneto hydro-dynamic (MHD) instability observed in tokamak operation when the q profile in the plasma core is close to unity. This MHD instability impacts both the transport of the bulk plasma (current, particle and energy transport) and minority species, such as fast ions. In TCV ($R_0/a = 0.88\,\text{m}/0.25\,\text{m}$) the fast ion population is generated in the plasma by neutral beam tangential injection of energies up to $28\,\text{keV}$. TCV features 16 active shaping coils permitting a great flexibility in plasma shape, including negative triangularity (δ) configurations that show surprisingly high confinement.

This study focuses on the transport of fast ions induced by sawteeth, by comparing two triangularity cases and simulation results with experimental data. Comparison of two equilibria with opposite δ shows that the fast ion drifts are larger for $\delta < 0$. Furthermore, the sawtooth-induced transport in this case is larger than $\delta > 0$ in similar conditions.

Comparison with experimental data confirms the dominance of the modification of thermal kinetic profiles following the sawtooth crash in explaining drops in the neutron rates and FIDA signals. Additional fast ion diffusion, however, improves the interpretation of the experimental data. For $\delta < 0$, the amplitude of the perturbation better representing the experimental data is larger. Finaly, an exploratory study for $50\,\text{keV}$ particles (soon available in TCV) shows that the situation does not worsen for such particles.

1 Introduction

Fast ions are a key ingredient to reach nuclear fusion in a magnetic confinement device. Fusion α-s will be the main actors to heat an ignited plasma and neutral beam injection is a common actuator for plasma heating in existing and future tokamak devices like TCV, JT-60 SA and ITER. A common instability in tokamak plasmas is the so-called *sawtooth*, which is a periodic magnetic reconnection event in the plasma core [1], [2]. It has a dramatic effect on bulk plasma confinement, resulting in a drop in central density and temperature. They also interact with fast ions, where the sawtooth period is seen to be modified in the presence of fast ions [3], [4], [5] and, conversely, where the fast ion transport deviates farther from neoclassical theory as shown theoretically and experimentally [6], [7], [8], [9].

The electric field caused by sawtooth crash is expected to induce additional fast ion transport. The electric field induced by the reconnection is expected to have a marginal role in the additional transport [10]. This transport leads to a drop in the fast ion content in the core, causing a decrease in fast ion density and stored energy, together with all the expected consequences (such as a drop in

the neutron rate). Three characteristic times are involved. τ_{CR}, the crash time, τ_{pr} the precession time of the fast ion around the toroidal direction and τ_{L} the longitudinal time (the time the particle orbits around a given flux surface). Toroidal precession tends to keep the particles at a constant radial position, whereas longitudinal motion moves them with displaced flux surfaces. If τ_{CR} is the shortest (i.e. the crash is the fastest event) then the particles are frozen in the flux surface and suffer high transport. This is the case for low-energy trapped particles. This criterion can be put in terms of the particle energy, defining a so-called *critical energy* [11], obtained by comparing the crash duration to the period of the toroidal precession of a well-trapped ion

$$E_{\mathrm{crit}} = 2\pi M k_s r_s R_0 \frac{\omega_B}{\tau_{\mathrm{CR}}} \tag{1}$$

where M is the fast ion mass, k the flux-surface elongation, r the normalized minor radius, s labels the last surface with $q = 1$, R_0 the major radius, $\omega_B = qB_0/M$ the cyclotron frequency and τ_{CR} the crash duration. For the cases considered in this work ($\omega_B = 72\,\mathrm{MHz}$, $k_s \sim 1$, $r_s \sim 0.2$, $\tau_{\mathrm{CR}} \sim 300\,\mu\mathrm{s}$), we obtain a critical energy of $\leq 10\,\mathrm{keV}$. For comparison, a JET-sized experiment has a critical energy of $\sim 300\,\mathrm{keV}$. If $E < E_{\mathrm{crit}}$, τ_{CR} dominates and thus fast ions are strongly transported away from the plasma core. In the case of particles with $E > E_{\mathrm{crit}}$, two separate cases must be considered. If $\tau_{\mathrm{pr}} > \tau_{\mathrm{L}}$, toroidal precession is too weak to decorrelate particle motion and the electric field, and fast ions suffer transport. When $\tau_{\mathrm{pr}} < \tau_{\mathrm{CR}}$ and $\tau_{\mathrm{pr}} < \tau_{\mathrm{L}}$ (mainly trapped particles), precession dominates and particles are decorrelated from the MHD-induced electric field, reducing such effects. Fast ion transport may also be induced by a fast ion-kink mode resonance, but this occurs at energies of the order of MeV.

Negative triangularity plasma configurations in a tokamak are becoming a possible reactor-device solution as access to H-mode, with the accompanying ELM events, is strongly reduced whilst retaining good energy confinement [12]. To date, TCV is the only device studying impact of extreme shaping on sawtooth instability [13], [14], where sawtooth period is seen to decrease with negative triangularity, that is related to the ideal nature of the mode. In this work we will assume that the magnetic reconnection associated to the sawtooth is negligible in causing additional fast ion transport [10].

In this work, the impact on fast ion confinement on TCV of positive and negative triangularity configurations is modeled in an attempt to interpret the experimental data. The stabilization of sawtooth crashes, provided by fast particles in different plasma configurations, is left for future activities.

The paper is structured as follows. Section 2 shows the orbit drifts in axisimmetric positive and negative triangularity, section 3 compares the additional fast ion transport from the internal kink mode for the two triangularities, section 4 presents the experimental data used to apply the model and a comparison of modelling and experimental data. Finally, section 5 presents the results for diffusion with injection of 50 keV particles.

2 Fast ion dynamics in axisimmetric positive and negative triangularity

In this first section, the features of the fast ion orbits of opposite δ axisimmetric equilibria is described.

The equilibria are designed to compare the fast ion behaviour in plasma configurations having same profiles, but opposite triangularity. In this way, the effect of shaping in the orbit drift is isolated. The CHEASE code [15] is used to construct the equilibrium for the plasma with positive triangularity ($\delta > 0$) from the experiment. The safety factor profile from this case is then used as input for an equilibrium with negative triangularity ($\delta < 0$). Equilibria with the same B_0, I_p, q profiles (mapped on the normalized poloidal flux variable), but opposite triangularity, were obtained (see figure 1a). The main difference lies in the poloidal flux function (F), as the plasma volume is distributed differently by the two shapes, that spans different regions of the toroidal field strength. This plasma current density distributions results in different F.

Three particles in passing orbits ($\mu \cdot B_0/E = 0.2$, $E = 20\,\mathrm{keV}$) at different starting ψ_0 (0.2, 0.5 and 0.8) are tracked in an axisymmetric simulation, neglecting collisions, figure 1b. The particle bounce time for $\delta < 0$ (black) is longer than for $\delta > 0$ (red). This can be explained by the change in plasma axis location. In the cases here explored, $R_{axis}^{\delta>0} = 0.90\,\mathrm{m}$ while $R_{axis}^{\delta<0} = 0.92\,\mathrm{m}$. This
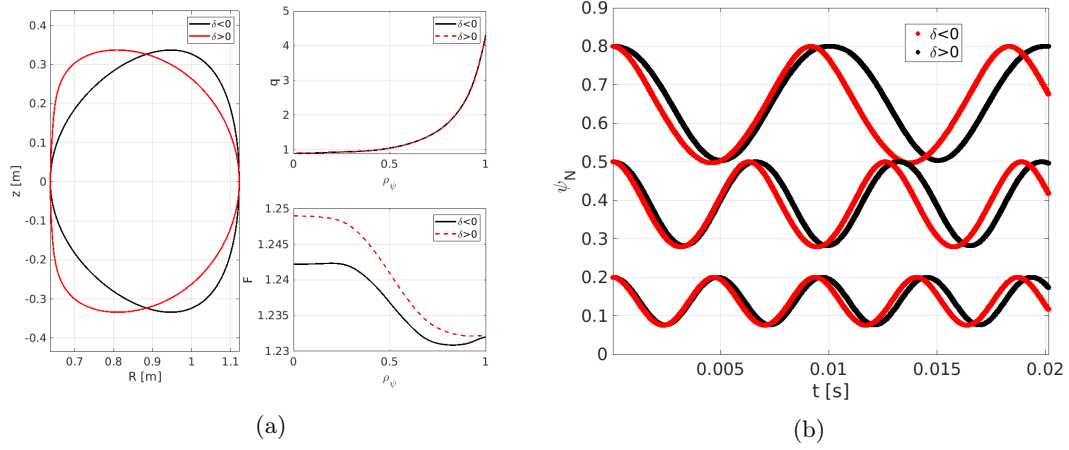
Figure 1: (a) Equilibria used to compare the additional fast ion diffusion in opposite triangularity. (b) the normalized toroidal flux ψ explored in the plasma by particles starting at different positions (point at t=0), in different equilibria (red: $\delta > 0$, black: $\delta < 0$)

change is only $\sim 2\%$ in the plasma axis location, with an impact of $\sim 4\%$ on the fast ion orbits bounce time as $\tau_B \sim R_0^2$ [16].

3 Modelling of the fast ion transport using the kick-model

3.1 Modelling of the magnetic perturbation

The ideal MHD perturbation has been modelled using the KINX code [17]. The perturbation in the cases here explored is assumed ideal as previously studied in [13] and we assume the linear MHD is sufficient to capture the interaction between sawteeth and fast particles. The equilibria (as in section 2) feature a $q < 1$ region from a kinetic equilibrium reconstruction for $\delta > 0$ case, engendering a the (1,1) mode. Its normalized radial displacement $\xi \cdot \nabla \psi$ (toroidal mode number $n = 1$, poloidal mode number $m = 1$) obtained by KINX for the two triangularities are shown in figure 2a. The perturbation maximum in $\delta < 0$ is slightly shifted inwards than $\delta > 0$ for the same q profile. The difference in plasma axis position (i.e. the magnetic field) and the current redistribution can explain the mode structure differences.
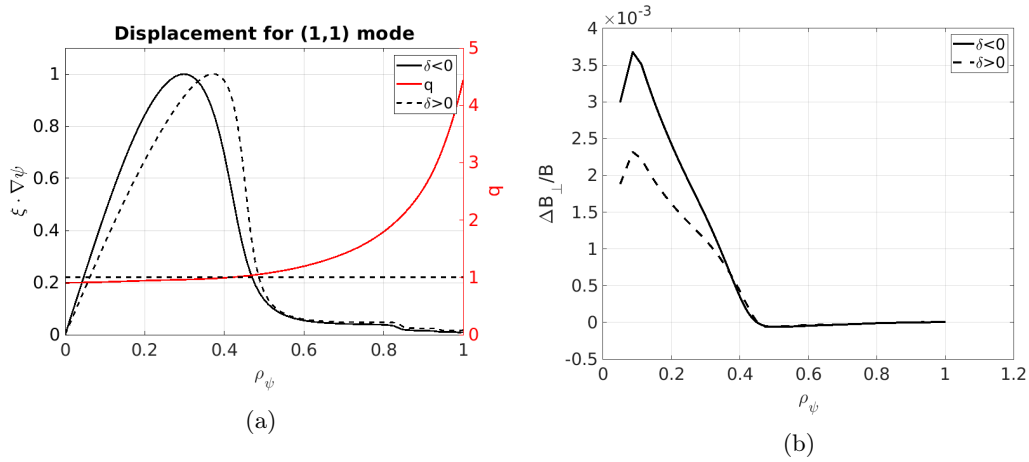

Figure 2: (a) Normalized $\xi \cdot \nabla \psi$ for the (1,1) mode computed by KINX in opposite triangularities (black solid: $\delta < 0$, black dotted: $\delta > 0$), at the same q profile (red). (b) radial magnetic field amplitude (normalized to the on-axis magnetic field) for the two different triangularities, with $A = 10^{-3}$

As introduced earlier, the relevant quantity for fast ion transport is the radial electric field,

3

which is computed from the the magnetic perturbation. Following the conventions in [18], a perturbed magnetic field (normal to the magnetic surfaces) can be expressed as:

$$\delta \vec{B} \cdot \nabla \psi_p = \sum_{m,n} \frac{mg + nI}{J} \alpha_{mn}(\psi_p) \cos(n\zeta - m\theta - \omega t) \tag{2}$$

where ζ and θ are the toroidal and poloidal angles, ω the mode frequency and J the jacobian for boozer coordinate conversion.

The α function is related to the radial displacement $\xi \cdot \nabla \psi$ obtained by KINX as follows

$$\alpha_{mn}(\psi_p) = \frac{m/q - n}{mg + nI} \xi_{mn}(\psi_p) \tag{3}$$

where ψ_p is the poloidal magnetic flux, m and n label respectively the poloidal and toroidal mode numbers, q is the safety factor, g and I are poloidal and toroidal current functions, following the same notation as [18].

As the perturbation $\xi \cdot \nabla \psi$ by linear MHD codes is obtained with normalized amplitudes, there is a free scaling factor (amplitude) to determine. In this section, the amplitude will be set to $A = 10^{-3}$ in order to simplify comparisons for opposite triangularities. The resulting perturbation (see figure 2b) is large enough to model its impact on the fast ion confinement whilst retaining the base magnetic configuration. For the comparison with experimental data, a sensitivity study with amplitude will be performed.

3.2 Modelling of the additional fast ion transport

The model for additional fast ion diffusion chosen for this work is the so-called kick-model [19], [20]. This model is implemented within TRANSP that allows the inclusion of fast ion transport induced by MHD modes in integrated transport modelling. This model was employed in previous works to correctly estimate the sawtooth additional fast ion diffusion on NSTX-U [8], [21].

In computing the diffusion matrix, we superimpose the equilibrium magnetic field with the magnetic perturbation computed by KINX and using equation 2, but only considering m=1 mode component. In this way the magnetic field is a snapshot of the maximal perturbation during a crash. To compute the effective transport, we do not include the mode evolution nor any stochastization of the magnetic field lines.

The relevant fast ion quantities which are perturbed by MHD are P_ϕ (normalized canonical angular momentum $P_\phi = (mRv_\phi - Ze\psi)/\psi_{\text{edge}}$) and the energy. Using orbit tracking codes (in this work, ORBIT [22]), fast particle orbits are then computed, and the probability for a particle to receive a *kick* in energy or P_ϕ is recorded. For each point in the E, P_ϕ and μ (normalized adiabatic invariant $\mu = (mv_\perp^2/2B_\phi) \cdot B_0/E$) space, the probability distribution for an orbit to be perturbed in energy or P_ϕ is described by a 5-D matrix, which can then be used within tools like TRANSP. For the cases of interest in this paper, an orbit-tracking time-step of 6 ns was chosen and the time over which to average the kicks is around 1 µs.

In figures 3 the poincare plots for the two configurations are shown, at the same amplitude $A = 10^{-3}$. Figure 3a shows a field-line mapping, where the island width is large, but not enough to destroy the magnetic field structure. In figure 3b a Poincarè plot for particles with $E = 20$ keV and $\mu B_0/E = 0.6$ (in this case, passing particles) is shown. Here, the islands in the topology develop, and are larger for $\delta < 0$.

The diffusion matrices are then computed with the same amplitude $A = 10^{-3}$. The average kick in energy close to the injection energy is shown in figure 4, in the constants-of-motion space. As expected, the perturbation lies close to the plasma center (i.e. close to the second order curve with axis in 0, representing the particles crossing the magnetic axis), and impacts mostly passing particles.

For $\delta < 0$, the perturbation is strongest for $0.3 < \mu < 0.7$ and $P_\phi > 0.3$. It features a secondary *band* where the amplitude is large, further from the plasma center ($P_\phi \sim 0.2$). For $\delta > 0$, the *band* close to the core appears to vanish, whereas the perturbation further from the core is similar to the $\delta < 0$ case.

A simplified understanding of the impact on the fast particle transport is shown in figure 5, where several of the fast ion-related profiles (density, current drive profile and power coupled to the mode) are shown. The decrease in fast ion density in the core in $\delta < 0$ is twice that for $\delta > 0$,
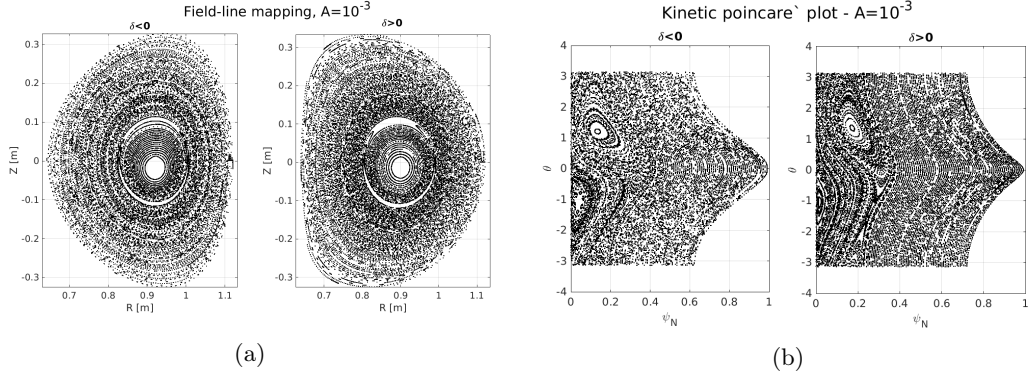
Figure 3: (a) Field line mapping of the perturbation in positive and negative triangularity. (b) Kinetic poincaré plot for a particle with $E = 20\,\text{keV}$ and $\mu B_0/E = 0.6$.
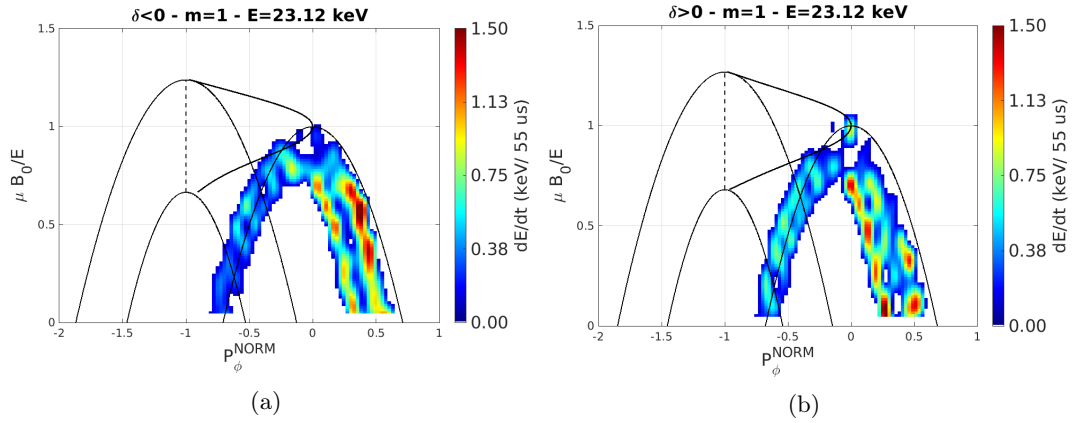

Figure 4: Intensity of the kicks in energy in positive and negative triangularity, considering only $m = 1$ component and an energy close to the injection energy. The black lines represent the constant of motion orbit boundaries.

and a similarly scaled effect is seen for the current density profile. The power coupled to the mode is larger (in absolute terms) across the whole plasma radius, consistent with the decrease in fast ion density profiles.

The impact on the fast ion profile is determined mainly by the modified magnetic perturbation. In support to this view, the equilibrium plasma shapes and the perturbation were mixed. The blue line in figure 5 shows the case for $\delta < 0$, but where the $\xi \cdot \nabla \psi$ for $\delta > 0$ was used. The transport remains similar to the $\delta > 0$ case.
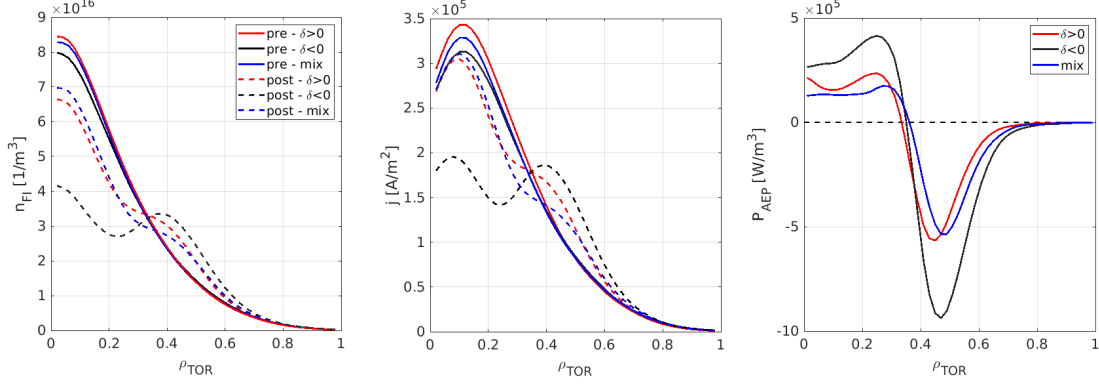
Figure 5: NB-related profiles before (solid) and after (dotted) the crash, for $\delta < 0$ (black), $\delta > 0$ (red) and a mix between negative delta shape but perturbation coming from the positive delta case (blue). Left figure is the fast ion density, center figure is the fast ion current drive, right figure is the power coupled between the fast particles and the mode.

The transport in (E, λ), E being the energy and λ the pitch angle (projection of the fast ion velocity on the magnetic field line) is shown in figure 6, at the position $(R, z) = (0.9, 0)$m. The phase space is filled using TCV NBH injected particles, thus regions at $\lambda \lesssim -0.5$ have a low number of markers. In subfigure (a) and (b) the equilibrium shape and the perturbation are consistent with each-other, showing that the perturbation is larger for $\delta < 0$ case. The perturbation impacts the same regions $|\lambda| \sim 0.5$, but in $\delta < 0$ it covers a larger energy range. In subfigure (c), the equilibrium plasma has $\delta < 0$, the perturbation is computed in $\delta > 0$ case. It can be noted the similarity between cases (c) and (b), confirming that also in this phase-space the perturbation (and not the equilibrium plasma shape) has the dominant effect on the additional fast ion transport.
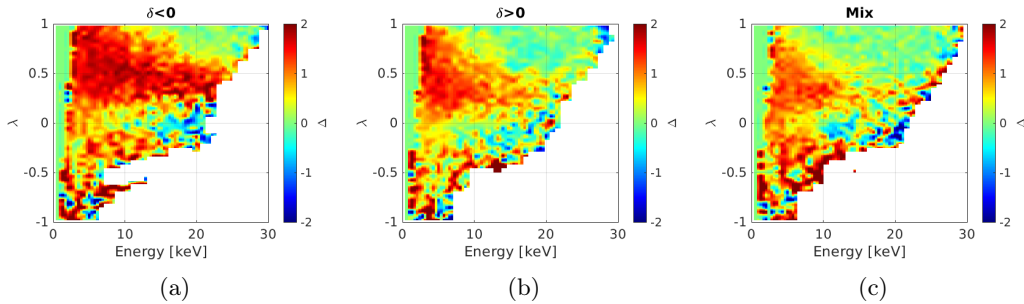

(a)   (b)   (c)

Figure 6: Difference in energy, pitch phase space at $(R, z) = (0.9, 0)$m, after and before the sawtooth crash, with three different perturbation. In cases (a) and (b) the perturbation is consistent with the plasma equilibrium, respectively $\delta > 0$ and $\delta < 0$. In case (c) the equilibrium has $\delta < 0$, the perturbation is computed in $\delta > 0$

Sawtooth crashes impact on fast particles is stronger for $\delta < 0$ rather than $\delta > 0$. The results here presented suggest that the fast ion sawteeth-induced transport is not determined by the plasma configuration, but rather by the magnetic perturbation. The larger magnetic perturbation is caused, in turn, by the change in plasma coverage of the toroidal field and changes in the current distribution profile. The deterioration of the fast ion confinement in the two different configurations is slightly linked to different neoclassical diffusion. The larger effect comes from the nature of the MHD perturbation, and not by a different interaction between fast ions and MHD activity.

4 Experimental observations

4.1 Experimental setup

Tokamak à Configuration Variable (TCV) [23] is a medium-size device ($R_0/a = 0.88\,\mathrm{m}/0.25\,\mathrm{m}$) capable of flexible plasma shaping due to 16 independent poloidal field coils and an over-sized vacuum chamber. Available heating systems include electron-cyclotron resonance heating and a 1.3 MW tangential neutral beam injector [24], [25] of D atoms with energies $\leq 30\,\mathrm{keV}$ (see figure 7a).

TCV is equipped with a large set of diagnostics. Electron density and temperature are measured by a Thomson scattering diagnostic, while the ion temperature and toroidal velocity by charge-exchange recombination spectroscopy. Interferometry is used to measure the line-averaged electron density with a time resolution capable to resolve the crashes. To study the fast ions, we focus on measurements taken with neutron detectors, fast ion D-α spectroscopy (FIDA) [26] and a compact neutral particle analyzer (CNPA). Figure 7a shows the lines-of-sight of CNPA and FIDA diagnostics together with the NBH central chord. The FIDA system has 10 lines of sight (LOS) with spatial resolution of $\sim 1\,\mathrm{cm}$ in radial direction observing the plasma high-field side midplane. The time resolution for the system is 1.3 ms which is fast enough to resolve the sawtooth-induced dynamics, that, with NBH injection, have a crash period of 10 ms. For each LOS (i.e. different radial position) we calculate FIDA intensity integrating the spectrum over the spectral range $[6524\,\text{Å}, 6545\,\text{Å}]$. This range contains mainly D_α emission from CX between NBH atoms and fast ions (defined as the 'active signal'). Through NBH modulation, a reference spectrum in the 'NBH-off' phase is subtracted from the spectrum obtained during the 'NBH-on' phase, such that the plasma conditions for both spectra match as well as possible. The CNPA was set to its most radial LOS for these experiments, with the plasma configuration chosen to avoid saturating of the high-energy ($> 20\,\mathrm{keV}$) channels.

This wide set of TCV fast-ion diagnostics allows the study of confinement in different phase-space regions.
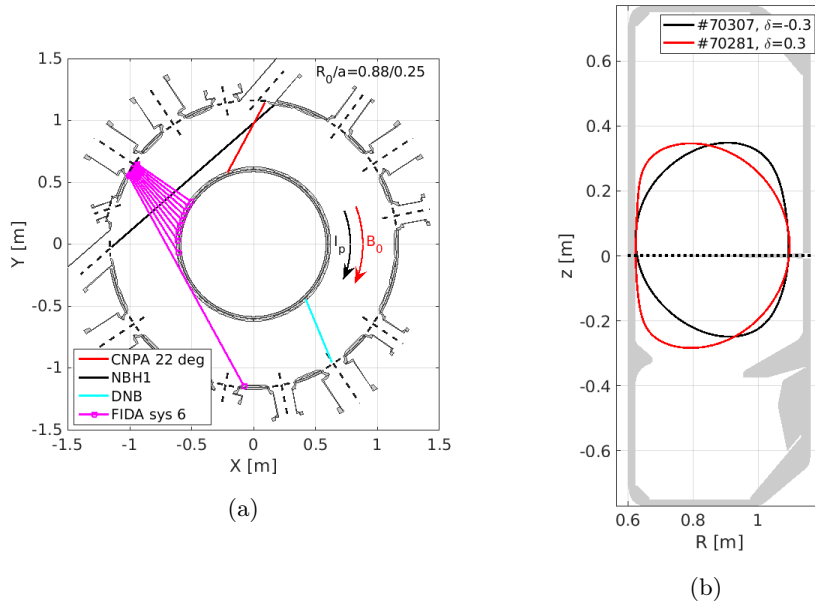

(a)

(b)

Figure 7: (a) Top view of TCV device. Magenta lines represent FIDA lines of sight. Black solid line is the approximate NBH injection line. (b) Plasma shapes used for this study. Dotted line at $z = 0\,\mathrm{m}$ is the injection geometry of the NBH, corresponding to the midplane

Two shots (#70307 with $\delta < 0$, #70281 with $\delta > 0$) were developed to compare the fast ion additional diffusion related to sawtooth crashes. The plasma current for both was 230 kA (figure 8a). Both shots have a symmetric shape in the poloidal plane (figure 7b), with an absolute triangularity $|\delta| = 0.3$. Both have the same NBH injected power (figure 8a) to simplify the neutron rate comparison. This choice, however, has the undesired consequences of non matched

kinetic parameters, due to the increased confinement with negative triangularity. Figure 8b plots the profiles as solid lines (black for $\delta < 0$ at $t = 1.3\,\text{s}$, red for $\delta > 0$ at $t = 0.7\,\text{s}$), with dotted black line reporting the $\delta < 0$ profiles at $t = 0.7\,\text{s}$ (lower NBH injected power). In the latter a better match is achieved within the two configurations, in particular concerning plasma electron density and ion temperature. In order to maximize neutron rates and compare similar fast ion populations, the selected time instants will feature the same NBH power in both configurations ($t_{\delta<0} = 1.3\,\text{s}$).
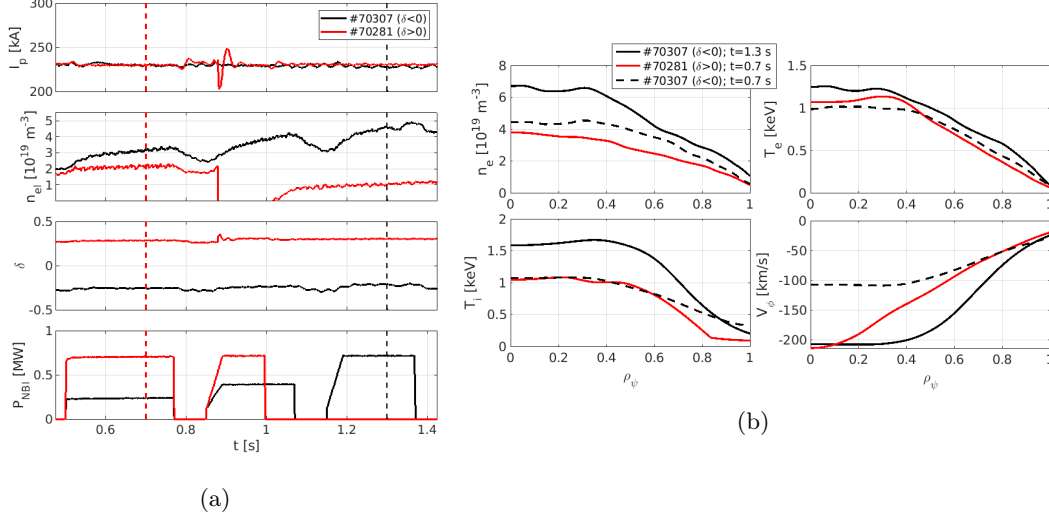

(a)

(b)

Figure 8: (a) time-traces for shots at positive (black) and negative (red) δ. Vertical dotted lines represent the instants for the profiles on figure (b). (b) kinetic profiles of the two shots showing n_e, $T_{e/i}$, V_ϕ at the two instants with different NB power (solid line). The dotted line is the $\delta < 0$ case at the same time point of $\delta > 0$ case.

We establish the relative changes caused by the sawtooth crashes in the FIDA and CNPA signals by calculating the fractional changes Δ_{FIDA} and Δ_{CNPA} between pre- and post-crash intensities. In the case of FIDA, for example, we define

$$\Delta_{\text{FIDA}} = \frac{I_{\text{post}} - I_{\text{pre}}}{(I_{\text{post}} + I_{\text{pre}})/2} \tag{4}$$

with the FIDA intensity, I, is obtained by integration of part of the FIDA spectra, as described above. The uncertainties in the FIDA measurements are calculated by considering both uncertainty due to the photon statistics and the detector read-out noise. Figure 9 shows the measurements of FIDA, CNPA and neutron rates. For both triangularities, the FIDA intensity decreases in the core after the sawtooth crash (figure 9a). An increase of roughly 10 to 40 % is seen also in the CNPA energy spectrum, at all the energies at the crash (figure 9b). Neutron rates have a higher time resolution with respect to CNPA and FIDA, so we can observe the drop in neutron rates much closer to the crash. A decrease of roughly 15% for $\delta > 0$ and 10% for $\delta < 0$ is seen following the crash (figure 9c), where the acquired signal maximum is normalized to 1.

4.2 Measurement of the (1,1) internal mode

The amplitude of the magnetic field perturbation was estimated from the standard pick-up coils and LTCC-3D diagnostic [27], [28]. The estimated radial magnetic field will be compared to that obtained using equation 2. To perform this estimation, we will assume only a $m = 1$ component (as in [8], [21]), that the magnetic field propagates in vacuum and a linear relation between the magnetic field's vertical and radial components.

In each experimental case, over a time window of 1 ms width enclosing a selected sawtooth crash, the MHD mode frequency is estimated by finding the related peak in the power spectral density. The field amplitude is then estimated by integrating the power spectral density in the selected frequency range. The toroidal mode number is determined with the phase of the fast
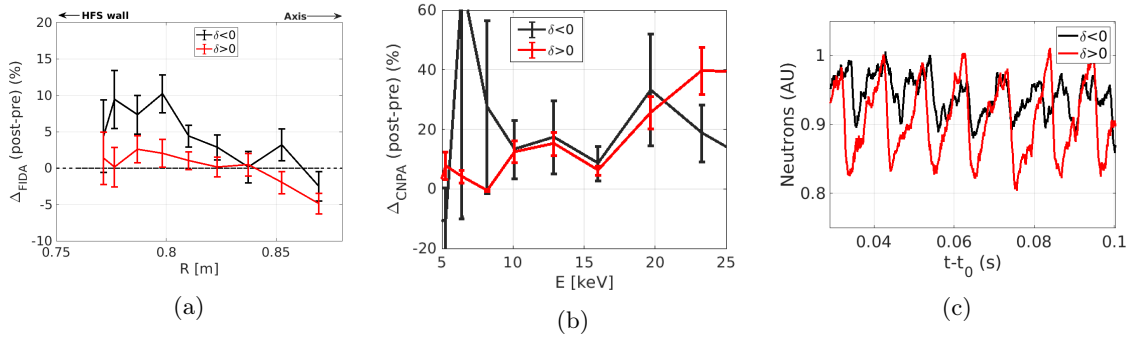
Figure 9: Experimental fast ion transport. (a) Δ_{FIDA} for each FIDA LOS plotted against the tokamak major radius (b) Δ_{CNPA} (c) is the neutron drop given by the sawteeth.

fourier transform of the coil arrays. From the frequency of the selected MHD mode, the radial magnetic field amplitude is computed in the same frequency range using the LTCC-3D signal.

The estimation of the mode structure employs the pick-up coils because of their larger coverage of the tokamak vessel (8 toroidal locations, while LTCC-3D are at only 3 toroidal locations). The dominant toroidal mode number, estimated from the pick-up coils, is $n = 1$, as expected. The selected mode frequency for $\delta < 0$ is $33\,\text{kHz}$, and $25\,\text{kHz}$ for $\delta > 0$. As expected, this frequency is close to the measured plasma rotation from CXRS. From the reasoning above, the peak in the frequency range selected is taken to come from the sawtooth perturbation, so the peak identification will also be used for the LTCC-3D coils.

In order to compare the estimated amplitude with the simulated one and since the probes are not at the last close flux surface (last point where the field can be simulated with the available tools) but at the vessel wall, the magnetic field at the last close flux surface is computed with the vacuum approximation (formula 5).

$$\delta B_{\text{LCFS}} = \delta B_{\text{wall}} \cdot \exp\left(\frac{R_{\text{wall}} - R_{\text{LCFS}}}{a}(1 + |m|)\right) \tag{5}$$

This is used to estimate the magnetic field component given by the internal kink mode, as shown in table 1. The first two rows display the poloidal magnetic field estimation by the two coil set. The LTCC estimation is clearly lower in the two cases. In the same frequency range, the LTCC-3D perpendicular field is computed (row 3). Assuming the $m = 1$ component dominates, it is possible to compute the field at the LCFS (row 4). Lastly, assuming proportionality between $B_\theta^{\text{pick-up}}$ (LFS) and B_θ^{LTCC} (LFS), the radial magnetic field at the LCFS is corrected (row 5). The last row shows the simulated radial magnetic field for $m = 1$ and $A = 10^{-4}$, which is of the same order of magnitude as the estimated one.

The estimated magnetic field amplitude in vacuum approximation (and assuming proportionality between the coil fields in different locations) is of the same order of magnitude as that computed from equation 2 with $A = 10^{-4}$. It is to be noted that the magnetic field perturbation is in general larger for $\delta < 0$ case, which would tend to imply a higher mode amplitude.

	70307 ($\delta < 0$)	70281 ($\delta > 0$)
$B_z^{\text{pick-up}}$(LFS)	$240.6\,\text{mG}$	$92\,\text{mG}$
B_z^{LTCC}(LFS)	$148\,\text{mG} \sim (B_z^{\text{pick-up}}(\text{LFS})/1.6)$	$75\,\text{mG} \sim (B_z^{\text{pick-up}}(\text{LFS})/1.2)$
$B_\perp^{\text{LTCC}}$	$18.35\,\text{mG}$	$7.2\,\text{mG}$
$B_\perp^{\text{LCFS}}$(m=1)	$29\,\text{mG}$	$13\,\text{mG}$
$B_\perp^{\text{LCFS}}$(m=1) corrected	$18\,\text{mG}$	$11\,\text{mG}$
$B_\perp^{\text{LCFS}}$(SIM, m=1, $A = 10^{-4}$)	$6.5\,\text{mG}$	$6.2\,\text{mG}$

Table 1: Qualitative estimation of the edge magnetic field caused by a selected sawtooth crash

4.3 Results and comparison with experimental data

Interpretative modelling of other experimental data is carried out with TRANSP and the kick-model's additional fast ion diffusion. The output distribution functions taken by the synthetic-diagnostic tool FIDASIM [29], [30] and compared to experiment. The combination of neutron rates measurements, FIDA and CNPA signals allows to validate the accuracy of the fast ion diffusion model and provide another estimation of the amplitude of the magnetic perturbation induced by sawtooth activity.

Changes to plasma bulk are included to help isolate the additional fast ion transport. Conditional averaging of the experimental Thomson scattering data points was performed on canonical crashes, (figure 10a), where the electron density is shown. The line-average shown is normalized to the fast interferometer measurement, in order to account for drifts in the line-averaged electron density. The profiles are similar and the densities are the same before and after the crash at $\rho_\psi = 0.35$ for both cases. We note that the drop in the core density for $\delta > 0$ (red lines) is larger than for $\delta < 0$ case. In the simulation, the background plasma modification is synced with the experimental sawtooth crashes and assumed to to remain the same throughout.

The magnetic perturbation is included within the simulations. The model can set a time-dependent mode amplitude and, in this case, we apply a step function of $200\,\mu s$ width around the experimental sawtooth crash time (initiated before the sawtooth crash). An example is shown in figure 10b. The fast ion diffusion matrices are taken similar to those shown in section 3.
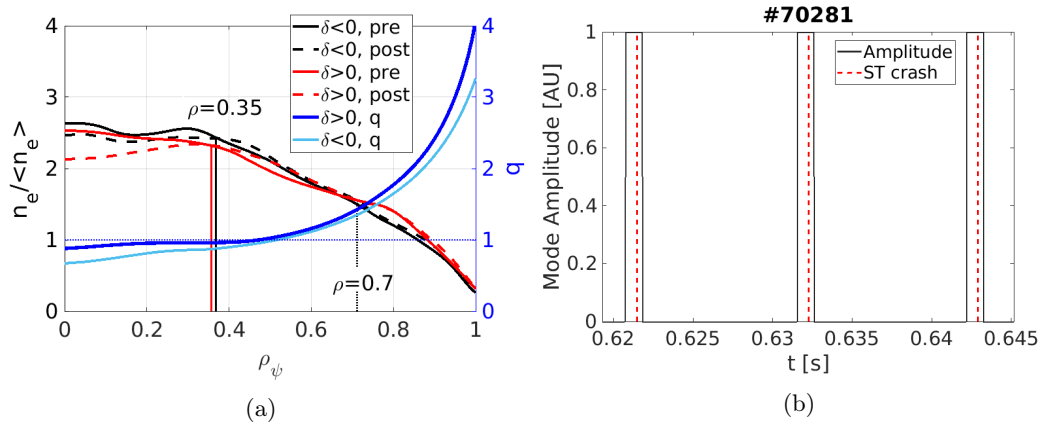

Figure 10: (a) fitted electron density (normalized to line-average density) before and after the sawtooth crash. Colors and symbols in the legend; (b) Amplitude of the perturbation as implemented in TRANSP

In figure 11 the neutron rates (normalized) from simulations are compared to experiment (black lines). The kinetic profile drops contribute greatly to the neutron changes (see curves with $A = 0$). The best match of the drop intensity for $\delta < 0$ is obtained with a magnetic field perturbation amplitude of $A = 10^{-4}$, whereas for $\delta > 0$ 10^{-5} is sufficient. These values are in agreement with the estimated amplitude from section 4.2. The kinetic profiles are obtained by conditional averaging over a series of crashes, thus for some single events the simulated neutron rate might have a different timescale with respect to the experiment, but on average there is sufficient agreement. A value of $A = 10^{-3}$ overestimates the neutron drop in both cases (in $\delta < 0$, reproduces the neutron drop without background plasma modification, see blue line in figure 11a).

The neutron drop rate alone can not be taken as conclusive, as several combinations of n_e and magnetic perturbation amplitude would give the same result. FIDA and CNPA signals are now compared to resolve this duality.

The sensitivity of FIDA and CNPA to the fast ion distribution function can be computed with FIDASIM. In figure 12 the diagnostics weight functions can be seen. It can be noted that they are mostly observing the passing particles high energy region.

In figure 13, simulated Δ_{FIDA} vs R_{major} are compared to measurements. The simulated values are obtained by integration of synthetic spectra (generated by FIDASIM) in the same wavelength range as for the experimental spectra. Figure 13a shows $\delta < 0$ results for the same cases as the neutron drop rates described above. Here, the simulation with $A = 10^{-4}$ and an appropriate background plasma agrees well with experiment. Without the magnetic perturbation, $A = 0$,
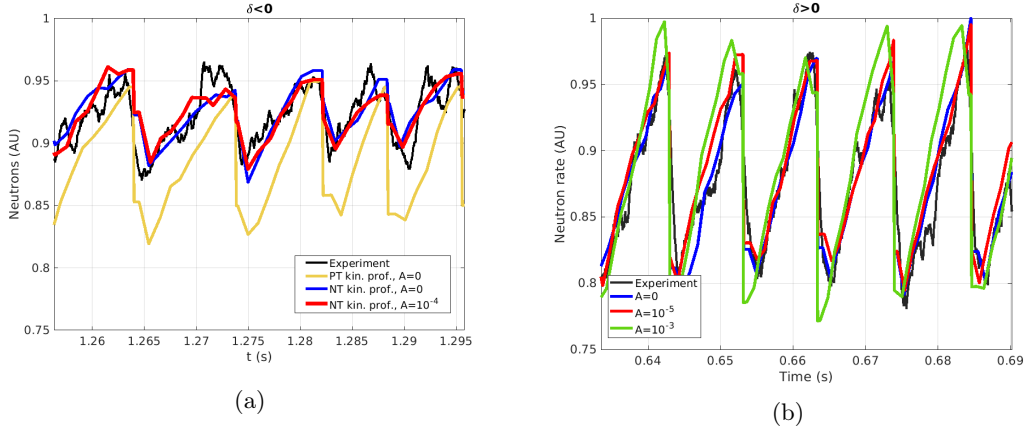
Figure 11: Drop in neutron rates after the sawtooth crash, compared to modelling. Black lines are the experimental data, colored lines are labeled in the legend

increases the simulated data closer to the core, as expected. The case with $A = 10^{-3}$ results in a too small fast ion content after the crash. A similar picture for $\delta > 0$ is presented in figure 13b, where $A = 0$ overestimates the post-crash FIDA signal in the core, $A = 10^{-3}$ underestimates the post-crash FIDA signal, while $A = 10^{-5}$ remains within the experimental error-bars even close to the plasma core.
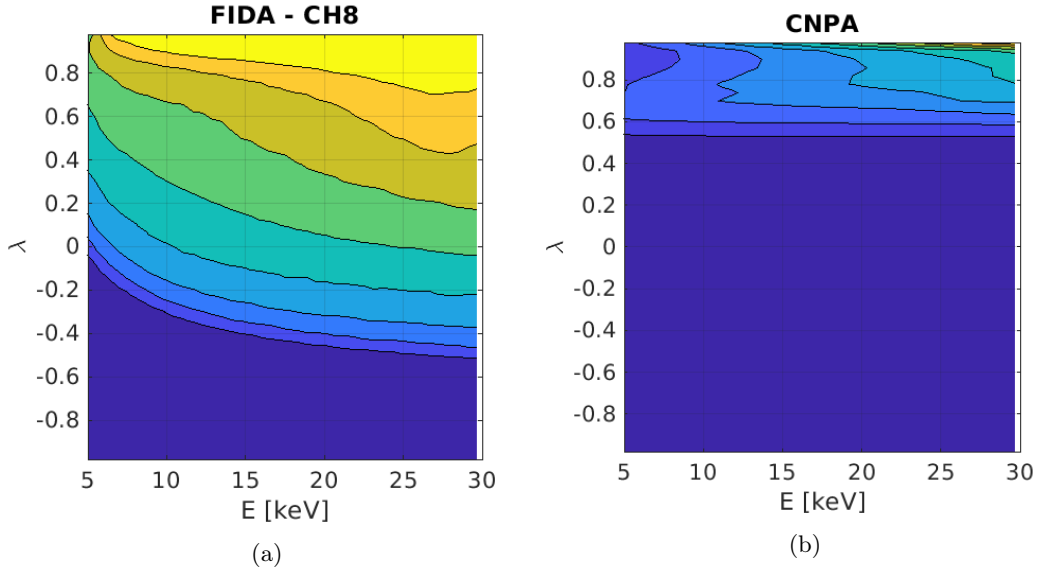

Figure 12: Example of fidasim weights for fast ion diagnostics. left: one FIDA channel; right: CNPA diagnostic. It can be noted that the diagnostics are mostly sensible to the passing particles high energy region

Finally, CNPA data is shown in figure 14. For $\delta < 0$ (figure 14a), the model with optimal neutron and FIDA matching slightly underestimates the CNPA signal difference. No large differences are seen with varying mode amplitude. A similar conclusion can be drawn for $\delta > 0$ case (subfigure b), where experiment is best reproduced for energies below 20 keV and $A = 10^{-5}$.

CNPA data are sensitive to the bulk neutral density, which varies because of the sawtooth crashes. FRANTIC [31] model implemented in TRANSP can model 1D transport of neutrals, and the differences in the neutral content before/after the crash are shown in figure 15. In this context, the difference arises because of changes in the bulk plasma, and it is larger for $\delta > 0$ case as the difference in background plasma profiles. Being included in TRANSP, this difference is included also in FIDASIM simulations when computing the FIDA spectrum. Unfortunately there are some effects that cannot be included so far in TRANSP simulations, and it is out of the scope
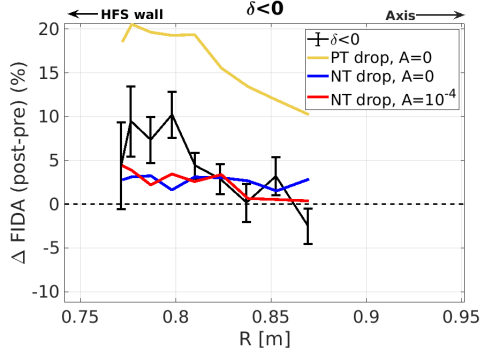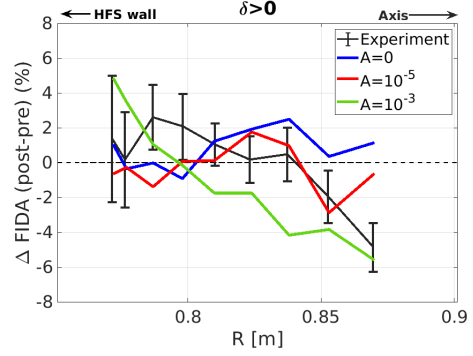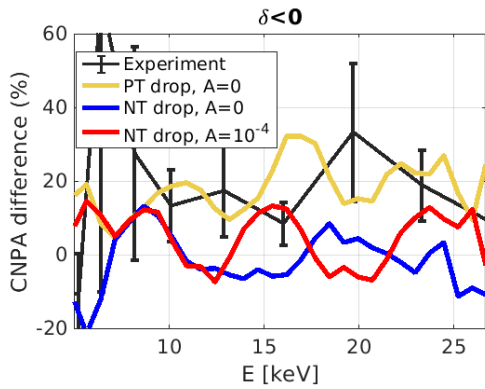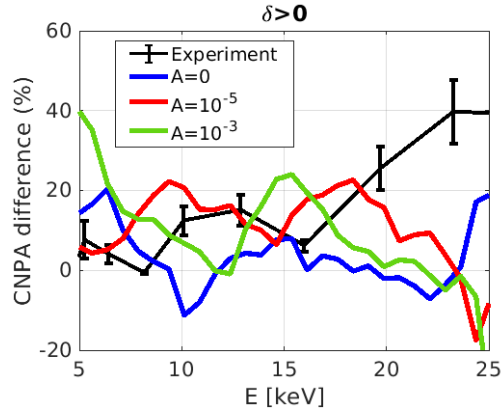
Figure 13: Difference in FIDA signal after the sawtooth crash, compared to modelling results obtained with FIDASIM. Black lines are the experimental data, colored lines are labeled in the legend

Figure 14: Difference in CNPA signal after the sawtooth crash, compared to modelling results obtained with FIDASIM. Black lines are the experimental data, colored lines are labeled in the legend

of this work to do so. The wall neutral source is included in our simulations by fixing the edge neutral density to the one estimated by baratron gauges. This gauge cannot capture edge neutral pressure modification because of the fast timescales of sawtooth crashes. In addition, the poloidal distribution of neutrals (in particular, between low-field side and high-field side) may be different for the two triangularities because of differences in machine wall clearances that will directly impact the CNPA signals. D-α signal spikes synchronized with sawteeth crashes were detected, but being the signal line-averaged it was not possible to include it in the simulations. Nonetheless, even if these effects can not be included in the simulations so far, the agreement with experimental data is satisfactory.
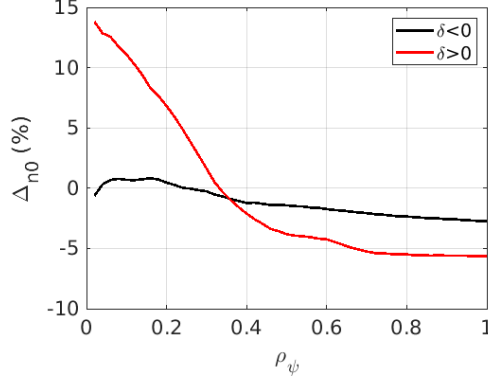

Figure 15: Neutral density difference before/after the crash as modeled by 1D FRANTIC model

The experimental data confirm additional fast ion diffusion resulting from the sawtooth crashes for $\delta > 0$ and $\delta < 0$. In similar conditions, the simulated radial magnetic field with $A = 10^{-4}$ is of the same order of magnitude as the estimated radial magnetic field, in both cases. Synthetic diagnostic modelling of neutron rates, CNPA and FIDA signal are also in qualitative agreement with the experimental data. A best match is obtained accounting for the main plasma variations with a perturbation amplitude of $A = 10^{-4}$ for $\delta < 0$, whereas $A = 10^{-5}$ is sufficient for $\delta > 0$. The background plasma is more modified by sawtooth crashes for $\delta > 0$, but fast ions suffer higher additional transport for $\delta < 0$ because of the nature of the interaction and the amplitude of the perturbation.

The presence of the additional fast ion transport caused by the sawtooth activity improves the agreement between experimental observations and modelling. However, for 25 keV particles in TCV, the dominant effect on synthetic diagnostic modelling comes from the modifications of the main plasma.

5 Extrapolation to $50\,\mathrm{keV}$ particles

TCV is being upgraded with a second NBI at 50 keV, with a similar injection direction and power as the first NBI (but opposite toroidal direction). In this section, predictive modelling of the deterioration of fast ion confinement for 50 keV particles is explored. The same beam configuration is retained, but the beam energy doubled. The kinetic profiles and magnetic perturbation amplitudes are assumed to be identical to those that best represent experimental data of section 4.3.

Figure 16 shows the fast ion density profiles before and after the crash for both triangularities. The density drop is larger for 25 keV particles with both δ. For 50 keV particles, for $\delta > 0$ there is little additional fast ion transport, and for $\delta < 0$ it is strongly reduced. For the latter the precession time is reduced together with the additional transport. Furthermore, energetic particles loss is significant from charge-exchange in TCV, so many particles do not slow down enough to interact with the mode.

A similar picture can be shown by looking at the maximum variation of the canonical angular momentum ΔP_ϕ, in figure 17. With a similar perturbation amplitude, the maximal ΔP_ϕ in both cases is in the order of 10^{-4}. For $\delta < 0$, figure 17a, the perturbation also has a large amplitude at $E = 50\,\mathrm{keV}$ so that the perturbation acts before the particle is lost. In $\delta > 0$ case, the perturbation is relevant below 20 keV. Here, fast ions are lost through charge-exchange before their interacting with the perturbation.
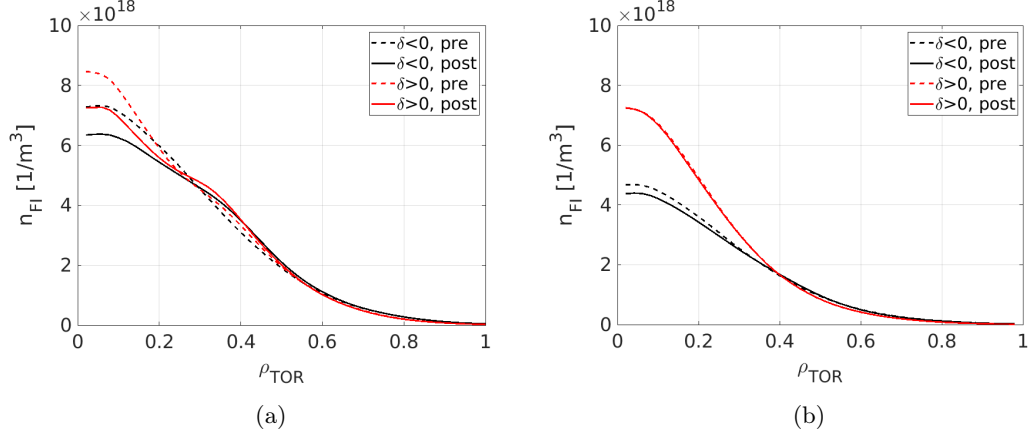
Figure 16: Predictive modelling of 50 keV particles. (a) n_{FI} at 25 keV for both δ before and after the crash (b) same figure with 50 keV particles
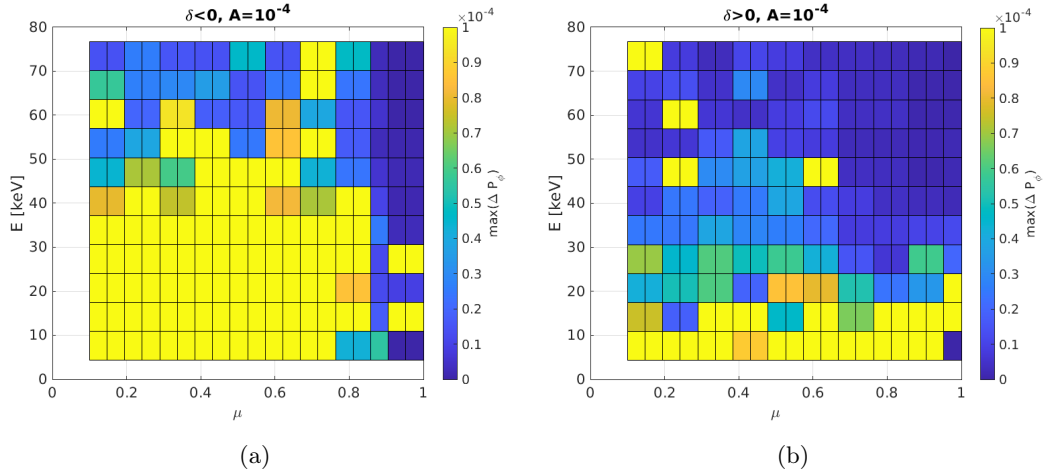

Figure 17: Maximum ΔP_ϕ as function of (μ, E). In $\delta < 0$ case (a), the perturbation reaches the injection energy (50 keV). In $\delta > 0$ case (b) the perturbation has its maximum below 20 keV.

This result is promising for future operation with high-energy neutral beam for TCV, where any increase in fast ion transport is predicted to be small. With the TCV NBH upgrade, an additional validation of the model will be possible based on the procedures outlined herein. The assumption of similar mode amplitude for the two beam energies requires confirmation with the help of experimental data, not yet available from TCV.

6 Conclusions

In this paper, additional fast ion transport generated by sawteeth crashes in TCV has been modelled using the kick-model in TRANSP, and the simulations compared against experimental data in cases with opposite triangularity.

Fast ion orbit bounce times in $\delta < 0$ are larger than for $\delta > 0$ with the same plasma equilibrium profiles. This results from differences in the Shafranov shift. This impacts the resonance condition that is of immediate interest when studying energetic particle resonance driven modes, such as toroidal Alfvén eigenmodes.

The (1,1) ideal magnetic perturbation, modeled using KINX code, shows an innermost peak for $\delta < 0$. This peak is closer to the core with respect to $\delta > 0$ configuration, and it may be caused by changes in plasma current density distribution and changes in the plasma axis location. This larger perturbation implies a larger fast ion transport for $\delta < 0$ that, in turn, impacts largely on the fast ion plasma content. In similar conditions, but opposite δ, the magnetic perturbation $\xi \cdot \nabla \psi$ dominates the fast ion transport, whereas the changes in equilibrium appear to play a marginal role.

Two plasma discharges were developed and diagnosed for comparison of the modelling results with experimental data. Difficulties in interpreting the FIDA data were seen due to strong modification of the $D - \alpha$ light induced by the sawtooth crash, partially invalidating the background subtraction correction for the FIDA spectrum. The neutron drop rates with $\delta < 0$ are smaller than $\delta > 0$ as the smaller background plasma changes. The estimation of the radial magnetic field amplitude from pick-up and LTCC-3D probes gave a qualitative trend that was close to a simulated scaling factor $A = 10^{-4}$. Including modifications of the plasma background resulting from sawteeth activity and this mode amplitude, it was possible to reproduce the experimental neutron drop rates and the FIDA radial profile drop for $\delta < 0$, while a smaller amplitude of $A = 10^{-5}$ was sufficient for $\delta > 0$. The results herein suggest that (a) crashes for $\delta < 0$ impact less on plasma performance (smaller neutron drop); (b) in TCV, the fast ion transport by sawtooth crashes is low in both cases, but for $\delta < 0$ the interaction between the mode and the fast particles is stronger. It is of interest to extend the results here obtained to other $\delta < 0$ devices, where the impact of the sawteeth on background plasma and the energetic particle phase-space filled through NBH will vary significantly.

In the final section, predictive simulation for $50 \, \mathrm{keV}$ ions were performed, that indicate that the change in kinetic profiles again dominates for the neutron rates, whereas fast ion transport is marginal. The magnetic perturbation has no time to impact on the fast ions, that are soon lost to other processes. In $\delta < 0$, ΔP_ϕ is larger at higher energies, leading to the conclusion that fast ion transport induced by sawteeth is higher in such conditions. The results obtained for $50 \, \mathrm{keV}$ particles will be validated against future experiments in TCV device.

Acknowledgments

References

[1] S. von Goeler, W. Stodiek, and N. Sauthoff. "Studies of Internal Disruptions and $m = 1$ Oscillations in Tokamak Discharges with Soft—X-Ray Tecniques". In: *Phys. Rev. Lett.* 33 (20 Nov. 1974), pp. 1201–1203. DOI: 10.1103/PhysRevLett.33.1201. URL: https://link.aps.org/doi/10.1103/PhysRevLett.33.1201.

[2] Boris B Kadomtsev. "Disruptive instability in tokamaks". In: *Fizika plazmy* 1 (1975), pp. 710–715.

[3] JP Graves et al. "Sawtooth control in fusion plasmas". In: *Plasma physics and controlled fusion* 47.12B (2005), B121.

[4] E Lerche et al. "Sawtooth control with modulated ICRH in JET-ILW H-mode plasmas". In: *Nuclear Fusion* 60.12 (2020), p. 126037.

[5] C Angioni et al. "Neutral beam stabilization of sawtooth oscillations in JET". In: *Plasma physics and controlled fusion* 44.2 (2002), p. 205.

[6] Ya I Kolesnichenko et al. "Effect of sawtooth oscillations on energetic ions". In: *Nuclear Fusion* 40.7 (2000), p. 1325.

[7] Yi Zhao and Roscoe B White. "Simulation of α-particle redistribution due to sawteeth on the tokamak fusion test reactor". In: *Physics of plasmas* 4.4 (1997), pp. 1103–1109.

[8] Deyong Liu et al. "Effect of sawtooth crashes on fast ion distribution in NSTX-U". In: *Nuclear Fusion* 58.8 (2018), p. 082028.

[9] Benedikt Geiger et al. "Fast-ion transport in the presence of magnetic reconnection induced by sawtooth oscillations in ASDEX Upgrade". In: *Nuclear Fusion* 54.2 (2014), p. 022005.

[10] Ya I Kolesnichenko et al. "Theory of fast ion transport induced by sawtooth oscillations: Overview and new results". In: *Physics of Plasmas* 4.7 (1997), pp. 2544–2554.

[11] Ya I Kolesnichenko and Yu V Yakovenko. "Theory of fast ion transport during sawtooth crashes in tokamaks". In: *Nuclear fusion* 36.2 (1996), p. 159.

[12] M Kikuchi et al. "L-mode-edge negative triangularity tokamak reactor". In: *Nuclear Fusion* 59.5 (2019), p. 056017.

[13] An Martynov, JP Graves, and O Sauter. "The stability of the ideal internal kink mode in realistic tokamak geometry". In: *Plasma physics and controlled fusion* 47.10 (2005), p. 1743.

[14] H Reimerdes et al. "Effect of triangular and elongated plasma shape on the sawtooth stability". In: *Plasma physics and controlled fusion* 42.6 (2000), p. 629.

[15] Hinrich Lütjens, Anders Bondeson, and Olivier Sauter. "The CHEASE code for toroidal MHD equilibria". In: *Computer physics communications* 97.3 (1996), pp. 219–260.

[16] LG Eriksson and F Porcelli. "Dynamics of energetic ion orbits in magnetically confined plasmas". In: *Plasma physics and controlled fusion* 43.4 (2001), R145.

[17] L Degtyarev et al. "The KINX ideal MHD stability code for axisymmetric plasmas with separatrix". In: *Computer Physics Communications* 103.1 (1997), pp. 10–27.

[18] Roscoe B White. "Representation of ideal magnetohydrodynamic modes". In: *Physics of Plasmas* 20.2 (2013), p. 022105.

[19] M Podestà et al. "Computation of Alfvèn eigenmode stability and saturation through a reduced fast ion transport model in the TRANSP tokamak transport code". In: *Plasma Physics and Controlled Fusion* 59.9 (2017), p. 095008.

[20] Mario Podesta, Marina Gorelenkova, and RB White. "A reduced fast ion transport model for the tokamak transport code TRANSP". In: *Plasma Physics and Controlled Fusion* 56.5 (2014), p. 055003.

[21] Doohyun Kim et al. "Investigation of fast particle redistribution induced by sawtooth instability in NSTX-U". In: *Nuclear Fusion* 59.8 (2019), p. 086007.

[22] RB t White and MS Chance. "Hamiltonian guiding center drift orbit calculation for plasmas of arbitrary cross section". In: *The Physics of fluids* 27.10 (1984), pp. 2455–2467.

[23] S Coda et al. "Physics research on the TCV tokamak facility: from conventional to alternative scenarios and beyond". In: *Nuclear Fusion* 59.11 (2019), p. 112023.

[24] Alexander N Karpushov et al. "Neutral beam heating on the TCV tokamak". In: *Fusion Engineering and Design* 123 (2017), pp. 468–472.

[25] M Vallar et al. "Status, scientific results and technical improvements of the NBH on TCV tokamak". In: *Fusion Engineering and Design* 146 (2019), pp. 773–777.

[26] WW Heidbrink et al. "Hydrogenic fast-ion diagnostic using Balmer-alpha light". In: *Plasma physics and controlled fusion* 46.12 (2004), p. 1855.

[27] Duccio Testa et al. "3D, LTCC-type, high-frequency magnetic sensors for the TCV Tokamak". In: *Fusion Engineering and Design* 96 (2015), pp. 989–992.

[28] D Testa et al. "LTCC magnetic sensors at EPFL and TCV: Lessons learnt for ITER". In: *Fusion Engineering and Design* 146 (2019), pp. 1553–1558.

[29] WW Heidbrink et al. "A code that simulates fast-ion Dα and neutral particle measurements". In: *Communications in Computational Physics* 10.3 (2011), pp. 716–741.

[30] B Geiger et al. "Progress in modelling fast-ion D-alpha spectra and neutral particle analyzer fluxes using FIDASIM". In: *Plasma Physics and Controlled Fusion* 62.10 (2020), p. 105008.

[31] S Tamor. "ANTIC: A code for calculation of neutral transport in cylindrical plasmas". In: *Journal of Computational Physics* 40.1 (1981), pp. 104–119.